

# The turbulent airflow over wind generated surface waves

M.P. Buckley<sup>a,\*</sup>, F. Veron<sup>b</sup>

<sup>a</sup> Institute of Coastal Research, Helmholtz-Zentrum Geesthacht, Max-Planck-Str. 1, 21502 Geesthacht, Germany

<sup>b</sup> School of Marine Science and Policy, College of Earth, Ocean and Environment, University of Delaware, Newark, DE 19716, USA

## ARTICLE INFO

### Article history:

Available online 18 April 2018

### Keywords:

Air–water interface

Wind waves

Wave–turbulence interactions

Airflow separation

## ABSTRACT

The airflow dynamics above the air–sea interface are believed to have a significant impact on the fluxes of momentum and scalars across the ocean surface. We present an experimental study of the turbulent structure of the airflow above wind generated surface waves. Measurements, taken at a fetch of 22.7 m in University of Delaware's large wind-wave-current facility, are reported for wind wave experiments with 10-m extrapolated wind speeds spanning from 2.19 m s<sup>-1</sup> to 16.63 m s<sup>-1</sup>. In order to complete this study, we developed a complex imaging system, combining particle image velocimetry with laser induced fluorescence techniques. High resolution two-dimensional (18.7 cm x 9.7 cm) velocity fields were measured as close as 100 μm above the air–water interface (on average). In addition, we acquired high spatial and temporal resolution wave field data simultaneously with the airflow measurements. Using this imaging system, we were able to perform phase averaging and separate the turbulent, mean and wave-induced velocity fields. We observe direct evidence of airflow separation events past the crests of wind waves, starting at low to moderate wind speeds ( $U_{10} > 2.19 \text{ m s}^{-1}$ ). In general, the turbulent boundary layer in the air is characterized by numerous velocity sweeps and ejections, accompanied by intense downwind-tilted spanwise vorticity (shear) layers stemming from the surface. We were able to directly observe these turbulent events, and estimate their statistical significance using quadrant analysis. These events become phase-locked in the presence of waves, and, when  $U_{10} \geq 5 \text{ m s}^{-1}$ , they are accompanied by intermittent airflow separation events past wave crests. The production of TKE also shows wave phase locked features indicating that further analysis of the wave-coherent contributions to the TKE balance is needed.

© 2018 The Authors. Published by Elsevier Masson SAS. This is an open access article under the CC BY-NC-ND license (<http://creativecommons.org/licenses/by-nc-nd/4.0/>).

## 1. Introduction

The dynamics of turbulent flows at gas–liquid interfaces are critical for a vast number of industrial and environmental systems. On the engineering side, such interfaces are commonly found in pipes (annular flows), in chemical reactors, condensers, boilers, turbines, etc. [1,2]. On the environmental side, at the air–sea interface, the complex feedback mechanisms involved in the coupling between wind and waves and their effects on the atmospheric and oceanic boundary layers have recently received increased interest, especially in the context of extreme weather forecasts. The development of extreme weather events and tropical storms, is in part dependent upon the drag (momentum flux) at the ocean surface [3–6]. At high wind speeds, the onset of sea spray generation is contingent upon breaking events and the wind shear at the ocean surface [7]. Ocean spray in turn contributes to the development of large storm systems, because it enhances latent and sensible heat fluxes at the air–sea interface [7]. In addition, the dynamics

at the air–sea interface are important for the transfer of gas across the ocean surface, which is significantly enhanced by the wave breaking and bubble entrainment events that occur at high wind speeds [8,9,7].

In spite of a large amount of existing literature on the topic of wind-wave interactions, the details of the coupled non-linear turbulent processes that take place within the coupled marine atmospheric and oceanic boundary layers are neither fully understood nor properly quantified, even in marginal wind conditions. Yet these coupled dynamics are pivotal for the generation and growth of waves by wind, the onset of wave breaking and the resulting dissipation of energy, the generation of marine aerosols under the action of wind and wave breaking and their influence on air–sea fluxes [10–13,8,14,7].

Current parametrizations of air–sea momentum fluxes are based on the “law of the wall”, relating the drag over a solid surface to its physical roughness, and identifying a self-similar log-linear velocity profile. Accounting for buoyancy effects results in the commonly used Monin–Obukhov similarity theory [15–19]. Over water however, the problem is more complex, since the wavy water surface is constantly moving and reacting to the overlying

\* Corresponding author.

E-mail address: [mbuckley@udel.edu](mailto:mbuckley@udel.edu) (M.P. Buckley).

airflow. The wind generates surface gravity waves, whose speed relative to that of the wind, or wave age  $C_p/u_*$  (where  $C_p$  is the speed of the dominant wave, and  $u_*$  the friction velocity of the air), strongly influences how the turbulent airflow is coupled with the wave field. Old swells may travel faster than the wind and cause upward turbulent momentum fluxes, while young, steep, strongly wind-forced waves lead to separated and non-separated sheltering of the airflow past wave crests, wave breaking, and aerosol generation [20–25,8,7,26,27]. The wave-induced modulations of the airflow turbulence, were identified by Hsu et al. [28] and later Belcher and Hunt [20] as a key component in the wind-wave coupling problem. However, due to the technical challenges involved, they have not, until now, been properly quantified experimentally. In addition, quantitative measurements of separated sheltering or airflow separation events, which are the air-side kinematic counterpart to wave breaking on the water side [29,30], and which arguably take place quite often over young strongly forced wind seas [26], remain scarce [31–34,26]. This is, in large part, due to the technical difficulties in measuring and modeling the complex multi-scale non-linear processes in the vicinity of a rapidly moving gas–liquid interface. Additionally, extracting turbulent quantities embedded within periodic wave-coherent motions is non-trivial [35–39].

In this paper, we measure and quantify the different components of the turbulent stress tensor in the airflow above young laboratory wind generated surface waves, using a high-resolution measurement system specifically developed for this study. We show the intense wave-phase-dependent modulation by the wave field, of the turbulence in the airflow, pointing to the importance of surface wave effects on the turbulent marine atmospheric boundary layer. The paper is organized as follows. After presenting the experimental setup, example high-resolution data products, and turbulence extraction methods in Section 2, we present and discuss phase-averaged results on the mean motions and turbulence in the airflow above laboratory wind waves, generated by mean 10-m wind speeds of  $U_{10} = 2.19, 9.41, \text{ and } 16.63 \text{ m s}^{-1}$  (Section 3). We summarize our contributions in Section 4.

## 2. Experimental setup and methods

The experiments presented here were performed in the 42m-long wind wave channel at the Air–Sea Interaction Laboratory of the University of Delaware. The channel is specifically designed for the study of air–water coupled wavy flows and air–sea interactions. It is 1 m wide, 1.25 m high, and was filled with fresh water up to a height of 0.7 m, leaving 0.55 m of air space. The sidewalls of the channel are made of glass to allow for non-intrusive optical measurements to be performed. For the study presented here, waves were naturally generated by the wind produced by a computer controlled, recirculating wind tunnel. We performed experiments with 10-m equivalent wind speeds  $U_{10}$  of 0.86,<sup>1</sup> 2.19, 5.00, 9.41, 14.34, and 16.63  $\text{m s}^{-1}$  and at a fetch of 22.7 m. Comprehensive results covering all wind speeds can be found in Buckley [40], Buckley and Veron [26]. Here, for the sake of brevity, we only show results for a representative sub-set of experiments, with  $U_{10}$  of 2.19, 9.41, 16.63  $\text{m s}^{-1}$  (see Table 1). For this study, focused on the turbulent airflow above surface waves, we developed a complex optical-imaging system. The apparatus combined Particle Image Velocimetry (PIV) and Laser Induced Fluorescence (LIF) measurements which allowed us to simultaneously measure two-dimensional velocity fields above a spatially resolved wind wave field. The system and data processing techniques are described in detail in Buckley and Veron [41]. Thus, we will present below only a short, summarized overview of the system and available data products.

<sup>1</sup> At the  $U_{10} = 0.86 \text{ m s}^{-1}$  wind speed, wind waves are not detected and the overall airflow resembles that over a solid flat plate, albeit with a slight drift at the interface.

### 2.1. Airflow velocity measurements

The airflow velocity measurements were obtained using a PIV setup which included two side-by-side 4 Mpix digital cameras (Jai RM4200, 2048 × 2048 pixels – 14.4 frames per second). A sketch of the setup is shown in Fig. 1. Images from these two cameras, were merged to obtain a single 18.7 × 9.7 PIV image with a final resolution of 47  $\mu\text{m}/\text{pixel}$ . The flow was seeded with 8–12  $\mu\text{m}$  water (fog) droplets which were illuminated by a laser sheet aligned with the along-wind direction in the center-line of the channel and generated by a pulsed Nd–Yag laser (New Wave Solo, 200 mJ per pulse). The resulting PIV image pairs were processed using a conventional cross-correlation algorithm utilizing increasingly smaller interrogation windows in order to optimize the measured velocity dynamic range [42]. The PIV system thus yielded 7.2 velocity maps per second with velocity vectors estimated on a physical grid size of 180  $\mu\text{m}$  in both horizontal  $x$  (along-wind) and vertical  $z$  directions.

In addition to the PIV, several optical LIF systems were utilized to detect the water surface in various ways. First, a 4 Mpix digital camera identical to that used for the PIV was positioned such that its field of view contained the merged PIV image. A trace amount of Rhodamine 6G added to the tank water was then excited by the PIV Nd–Yag laser such that the light emitted by the fluorescent dye could be imaged by the LIF camera. The LIF camera was also fitted with an optical filter which removed the green laser light scattered by the PIV particles thus providing crisp images of the fluorescent dye only. These LIF images provided images of the wavy surface from which a wave profile could be extracted (we named it PIV SD, for Surface Detection, in Fig. 1). This technique is similar to that described in [43] used to image surface wave profiles. In our case, we used these wave profiles to precisely locate the interface within the PIV field of view.

Fig. 2 shows instantaneous velocity fields obtained with the PIV system described above, and plotted over LIF images that yielded the position of the interface. Here, the first column of panels shows vector fields (decimated for clarity) where the colors denote  $|\mathbf{u}|$ , the magnitude of the measured airflow velocity. The adjacent panels show both the horizontal component,  $u$  and vertical component  $w$  of the measured velocity field  $\mathbf{u}$ . The three rows of panels correspond to 10-m equivalent wind speeds  $U_{10}$  of 2.19, 9.41, and 16.63  $\text{m s}^{-1}$ . These instantaneous horizontal velocity fields are typical and representative pictures of the airflow dynamics upwind and downwind of crests, above waves at the peak of the spectrum. The airflow exhibits notable differences as the wind speed increases. At  $U_{10} = 2.19 \text{ m s}^{-1}$ , only slow, low amplitude waves are generated. And while waves are present and deform the interface, the turbulent airflow presents similarities with that over a flat plate. Within the buffer layer, low velocity fluid is intermittently being ejected from the near surface region (Ejections, or Q2 events, see below) and higher velocity fluid is swept down toward the interface (Sweeps or Q4 events). Such sweeps and ejections events are characteristic of near-wall regions in turbulent boundary layers over rigid flat plates [e.g., 44–46]. At higher wind speeds, these events are less readily apparent and give way to what appears to be clear airflow separation from the interface. We note however that identifying airflow separation is not trivial and generally not possible from velocity measurements alone [47,33,34,26].

### 2.2. Surface wave measurements

A second, separate LIF system was used to obtain surface wave measurements. It comprised a 4 Mpix digital camera (Jai RM4200, 2048 × 2048 pixels - 7.2 frames per second) fitted with a 14 mm lens, resulting in a field of view covering 51.2 cm in the along

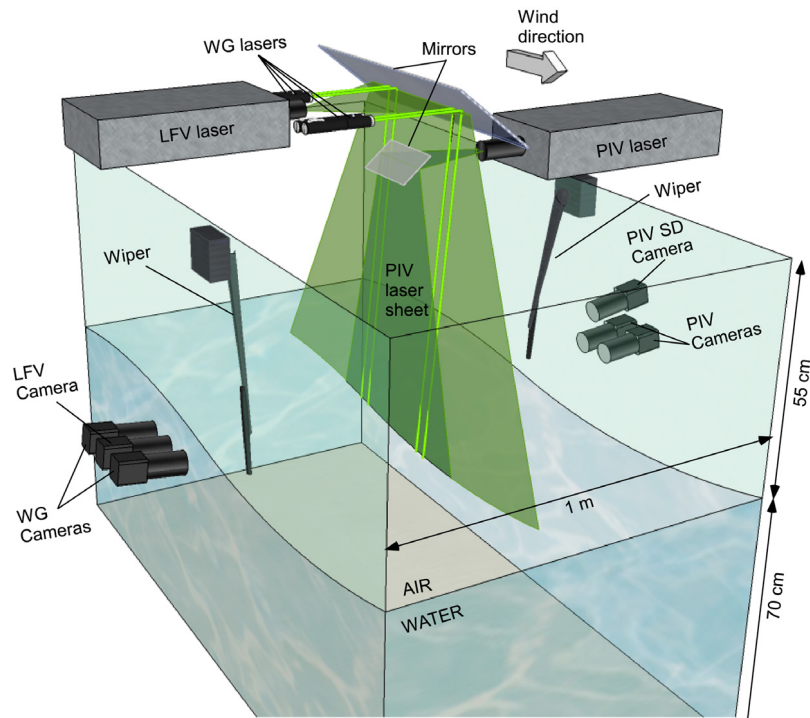


**Fig. 1.** Three-dimensional sketch of the experimental setup at the University of Delaware's air-sea interaction tank. The setup was placed at a fetch of 22.7 m. The airflow velocity measurement system (PIV), on the left side of the downwind direction, shows the PIV laser, PIV cameras, and surface detection camera (dubbed PIV SD). The wave measuring system is placed on the right hand side of the tank and comprises a large field of view (LFV) illumination laser sheet, a digital camera, single point wave gauge (WG) laser beams and two high speed imagers.

**Table 1**

Summary of experimental conditions. For each experiment, the friction velocity  $u_*$ , the 10-m extrapolated velocity  $U_{10}$ , and the wall-normalized roughness parameter  $z_{0+} = u_* z_0 / \nu$  (where  $z_0$  is the roughness length) were computed by fitting the logarithmic part of the averaged PIV velocity profile in the air. Peak wave frequencies  $f_p$  were obtained from laser wave gauge frequency spectra (WG). Other parameters with subscript  $p$  were derived by applying linear wave theory to  $f_p$ . The wave amplitude  $a_p$  was obtained from root-mean-square amplitude  $a_p = \sqrt{2} a_{rms}$  computed from the WG water surface elevation time series. The wall-normalized critical height is given by  $\zeta_{c+} = u_* \zeta_c / \nu$ , with  $\bar{u}(\zeta_c) = C_p$ .

$U_{10}$ m s <sup>-1</sup>	$u_*$ cm s <sup>-1</sup>	$z_{0+}$	$C_p$ m s <sup>-1</sup>	$C_p / u_*$	$a_p$ cm	$\lambda_p$ m	$a_p k_p$	$f_p$ Hz	$\zeta_c$ mm	$\zeta_{c+}$
2.19	7.3	0.21	0.47	6.5	0.15	0.14	0.07	3.3	1.84	9.0
9.41	31.4	0.96	0.78	2.5	1.20	0.39	0.19	2.0	0.33	6.9
16.63	67.2	17.68	0.92	1.4	2.29	0.54	0.27	1.7	0.38	16.8

channel direction (see Fig. 1). The fluorescent dye in the water was excited by a large laser sheet also aligned in the center-line of the channel and generated by a pulsed Nd-Yag laser (New Wave Solo, 120 mJ per pulse). The LIF images obtained with this system yielded profiles of the wavy surface over a larger footprint than that obtained from the PIV system and thus allowed for the wave field to be resolved substantially upwind and downwind of the PIV imaging area. In Fig. 1, the label “LFV” stands for Large Field of View and refers to this system. This large along-wind footprint allowed for Fourier modal analysis of the surface to be performed. In turn, this gave us the ability to (1) construct a meaningful surface-following coordinate system and (b) perform phase averaging to extract the turbulent velocity fields from instantaneous measurements (see Buckley and Veron [41] and below).

Finally, four single point optical wave gauges (noted WG) provided time series of the water height at single points positioned 2.8 and 1.4 cm upwind and 2.7 and 4.2 cm downwind of the PIV imaging area. These optical wave gauges also relied on LIF measurements performed with digital cameras operating at 93.6 Hz with a vertical resolution of 65  $\mu\text{m}$  per pixel. The fluorescent dye was excited using 4 continuous, single beam, 200 mW green laser pointers. These single point wave gauge measurements provided the peak wave frequencies reported in Table 1.

### 2.3. Coordinate transformation

Using the LIF surface wave profiles obtained over the large 51.2 cm field of view, at each time  $t$ , we decompose the water surface elevation  $\eta(x, t)$  into its spatial Fourier components

$$\eta(x, t) = \sum_n \sigma_n(x, t), \quad \text{with } \sigma_n(x, t) = a_n(t) e^{i(k_n x + \phi_n)}, \quad (1)$$

and where  $a_n$ ,  $k_n$ , and  $\phi_n$  are respectively the amplitude, wave number, and phase of  $\sigma_n$ , the  $n$ th mode of the Fourier decomposition. From there, we define a vertical coordinate  $\zeta$  which follows the surface near the surface, and tends toward the Cartesian  $z$  coordinate away from the surface and the influence of the waves. Accordingly,

$$\zeta = z - \sum_n \sigma_n(x, t) e^{-k_n \zeta}. \quad (2)$$

The rate at which the curvilinear system converges toward the Cartesian system is proportional to the wavenumber  $k_n$  of each wave mode. This is similar to the coordinate transformation recently used by Hara and Sullivan [48]. Since wind waves contain several Fourier modes, the locus of each constant vertical coordinate  $\zeta$  also contains several modes. Higher order modes (large

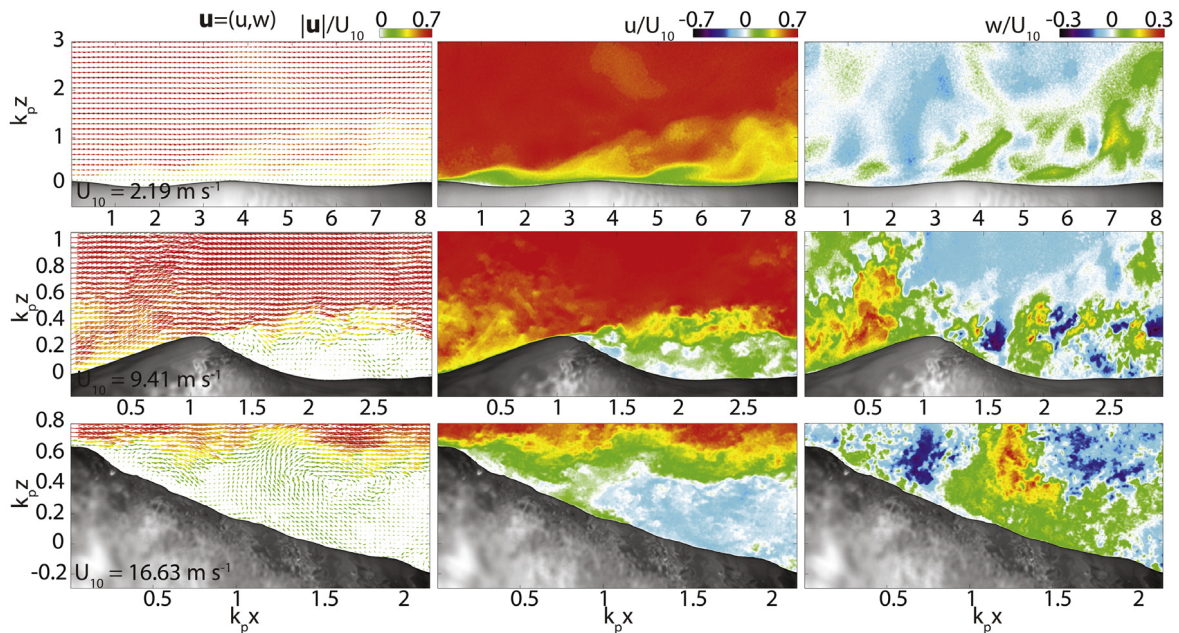


**Fig. 2.** Instantaneous velocity fields obtained with the PIV system for  $U_{10}$  of 2.19, 9.41, and 16.63  $\text{m s}^{-1}$ ; the wind speed is indicated in the first panel of each row. The first column of panels shows instantaneous velocity vector fields. For clarity, less than 10% of measured vectors are shown. The second and third columns show the horizontal  $u$  and vertical  $w$  components of the velocity vector  $\mathbf{u}$  respectively. Velocities are normalized by the 10-m wind speed  $U_{10}$ , and plotted above the surface image collected by the LIF camera. The vertical and horizontal axes are non-dimensionalized by the wavenumber of the peak surface wave.

wavenumbers) decay faster than lower order modes. So, close to the surface,  $\zeta$  follows the wavy surface accounting for the small scale spatial variability. In fact, the line  $\zeta = 0$  yields  $z = \eta(x)$  exactly. But, away from the surface, only the influence of the longer waves will be accounted for to estimate the height  $\zeta$  above the surface. This is physically intuitive and it is similar to how wave orbital velocities are confined near the interface. Here, this coordinate system simply accounts for the fact that longer waves influence the airflow up to a higher altitude than shorter waves do. Fig. 3a shows the coordinate  $\zeta$  overlaid on the instantaneous horizontal component  $u$  of the velocity.

#### 2.4. Phase-average and velocity decomposition

Again, by using the LIF surface wave profiles obtained over the large 51.2 cm field of view, we were able to estimate the local phase of the peak surface waves along the wave profile using Hilbert transform techniques (see Buckley and Veron [41] for details). Thus, local phases  $\phi$  (relative to the peak wave) could be determined for along-wind positions  $x$  along the wavy interface; in that sense, in what follows,  $\phi$  and  $x$  are interchangeable. Thus, instantaneous velocity profiles  $\mathbf{u}(x, \zeta)$  (profiles along  $\zeta$  at downwind position  $x$ ) obtained from many individual PIV realizations could be binned according to their phase  $\phi$ , then averaged. When repeated over the whole range of phases between  $-\pi$  and  $\pi$ , this yielded a phase-mean denoted  $\langle \mathbf{u} \rangle(\phi, \zeta)$ . Furthermore, individual, instantaneous velocity fields  $\mathbf{u}(x, \zeta)$  can be decomposed, as in a standard Reynolds decomposition, in the sum of a mean (here a phase-mean) and a turbulent deviation [e.g., 49,50,28]:

$$\mathbf{u}(x, \zeta) = \langle \mathbf{u} \rangle(\phi, \zeta) + \mathbf{u}'(x, \zeta). \quad (3)$$

Turbulent velocities are therefore obtained by subtracting  $\langle \mathbf{u} \rangle(x, \zeta)$  from instantaneous fields  $\mathbf{u}(x, \zeta)$ .

Fig. 3 shows the application of Eq. (3). Here, we show the turbulence extraction for an instantaneous velocity field at  $U_{10} = 9.41 \text{ m s}^{-1}$ . The wave-phase-averages  $\langle u \rangle$  and  $\langle w \rangle$  are plotted over

the instantaneous wave profiles.<sup>2</sup> In the streamwise direction,  $\langle u \rangle$  shows the thinning of the boundary layer upwind of the wave crest and sheltering effect downwind [21]. This effect is particularly clear on the velocity profiles overlaid on the panel showing  $\langle u \rangle$ . In the vertical direction,  $\langle w \rangle$  shows the effect of the waves, which, for this young, strongly wind-forced wave, deflect the flow upward on the upwind side of the crest and downward on the downwind side. Along-wave profiles of  $\langle w \rangle$ , plotted at constant heights  $\zeta$ , clearly show the deflection of the flow, and also show that the influence of the wave on the mean flow decreases away from the interface. Note here that the horizontal and vertical axes have been normalized with the peak wavenumber.

### 3. Results

#### 3.1. Mean velocity

The phase-averaged velocity fields  $\langle \mathbf{u} \rangle$  are employed to extract the turbulence from every individual PIV measurement but it is also useful to examine mean fields on their own. Fig. 4 shows phase-means for  $U_{10}$  of 2.19, 9.41, and 16.63  $\text{m s}^{-1}$ . Here, we have plotted these phase-means as a function of the wave phase and over the phase-averaged surface. The normalized streamwise phase-averaged velocity  $\langle u \rangle / U_{10}$  is shown in panels a, b, c of Fig. 4. In all three wind conditions, the horizontal velocity increases on average upwind of wave crests, and decreases downwind. This type of behavior was already visible in the instantaneous realization shown on Fig. 3. Individual profiles of  $\langle u \rangle / U_{10}$  are also plotted, at four different phases along the wave ( $\phi = -\pi/2, 0, \pi/2, \pi$ ). They emphasize the wave-induced modulations of the airflow boundary layer: Along the upwind face of waves, the boundary layer thins (the mean profile is “full” down to the water surface), whereas downwind of waves, the boundary layer thickens (the

<sup>2</sup> As mentioned earlier, instantaneous phase detection allows for  $x$  and  $\phi$  to be interchangeable; for convenience, we have plotted the phase of the wave profile underneath the  $x$ -axis.

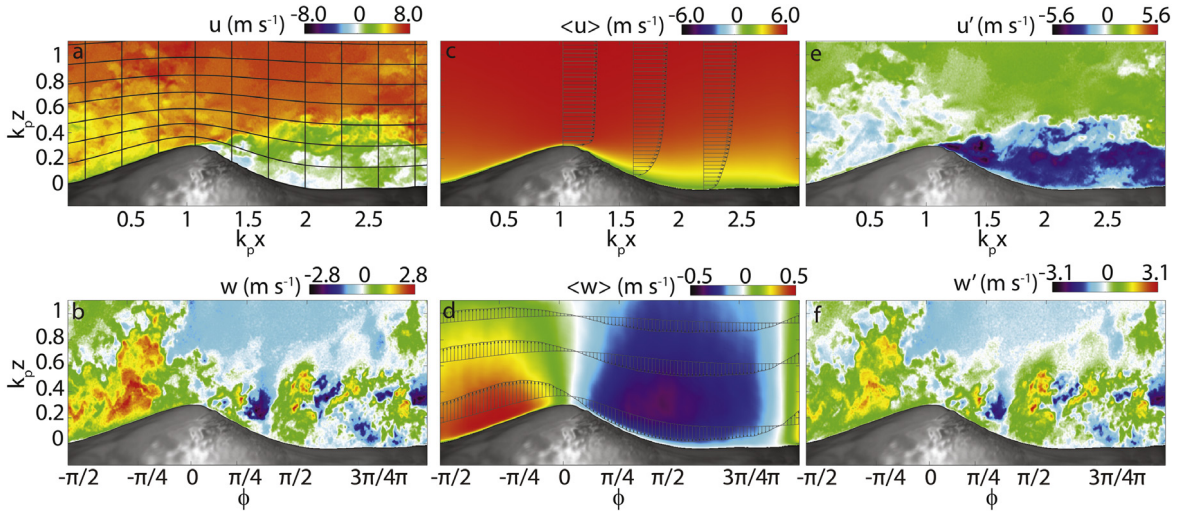


**Fig. 3.** Example of an instantaneous velocity field for  $U_{10} = 9.41 \text{ m s}^{-1}$  for which the Reynolds decomposition of Eq. (3) has been applied, yielding the turbulent velocity fields. The decomposition is applied to both measured components of the vector  $\mathbf{u}$ . Here,  $\langle \mathbf{u} \rangle$  is plotted over the instantaneous measured wave profile, that is as a function of  $x$  rather than a function of the local wave phase  $\phi$ . For reference,  $\phi$  is shown on the bottom horizontal axis. The wave-following vertical coordinate of Eq. (2) is also shown on panel a.

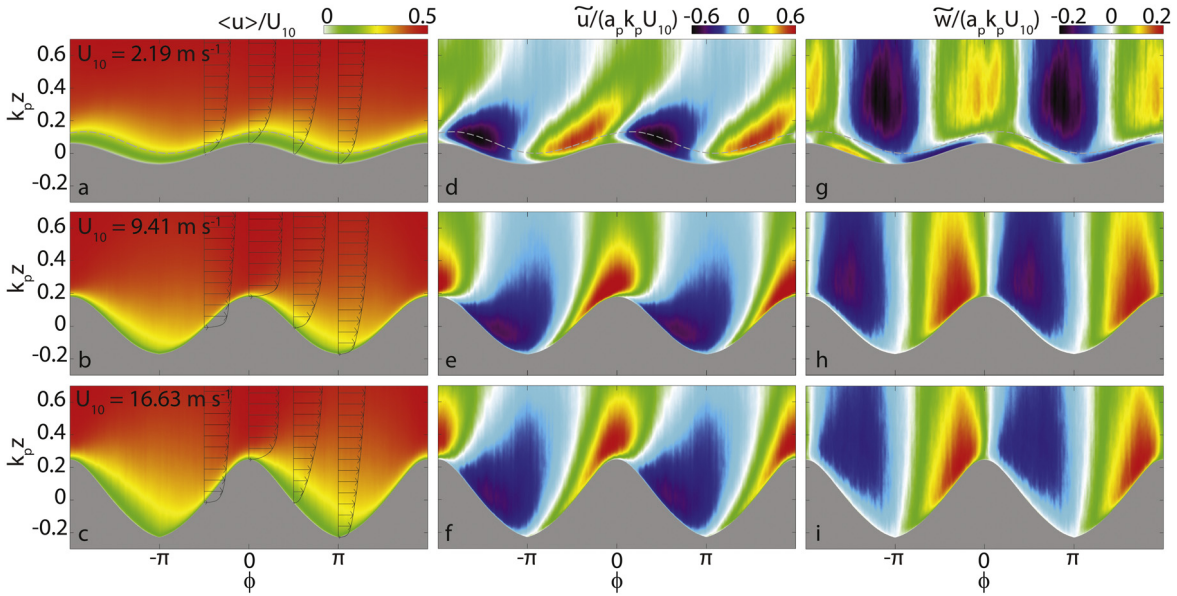


**Fig. 4.** Normalized phase-averaged velocities plotted over the phase-averaged surface elevation for  $U_{10}$  of 2.19, 9.41, and 16.63  $\text{m s}^{-1}$ . The left panels show the horizontal velocity component  $\langle u \rangle / U_{10}$ . The second and third columns show the normalized components of the wave coherent velocity  $\tilde{\mathbf{u}}$ . The dashed gray line represents the height of the critical layer, where the phase averaged horizontal airflow velocity  $\langle u \rangle$  matches the peak wave phase velocity  $C_p$ . Note that for the vertical direction,  $\tilde{w} = \langle w \rangle$ .

mean velocity profile is less full). To further examine the effect of the waves, we decompose the phase-averaged velocity fields  $\langle \mathbf{u} \rangle$  into the sum of an ensemble mean  $\bar{\mathbf{u}}$  (an average over all phases), and a phase-dependent, or wave-coherent deviation  $\tilde{\mathbf{u}}$ . In other words,

$$\langle \mathbf{u} \rangle(\phi, \zeta) = \bar{\mathbf{u}}(\zeta) + \tilde{\mathbf{u}}(\phi, \zeta), \quad (4)$$

which naturally leads to the following triple decomposition:

$$\mathbf{u}(x, \zeta) = \bar{\mathbf{u}}(\zeta) + \tilde{\mathbf{u}}(x, \zeta) + \mathbf{u}'(x, \zeta) \quad (5)$$

It should be noted that in order to define  $\bar{\mathbf{u}}$  and  $\tilde{\mathbf{u}}$  near the wind-forced wavy boundary, it is in fact necessary to use a wave-following vertical coordinate  $\zeta$ , otherwise,  $\mathbf{u}(z)$  at a fixed height  $z$  would alternatively be in the air or in the water when  $z$  approaches the interface. In panels d through i of Fig. 4, we show

the normalized wave-coherent velocity components  $\tilde{u}/(a_p k_p U_{10})$  and  $\tilde{w}/(a_p k_p U_{10})$ , resulting from such a decomposition. Here, 2 different types of patterns appear: At the two highest wind speeds ( $U_{10} = 9.41, 16.63 \text{ m s}^{-1}$ ), the airflow is deflected upward (resp. downward) and accelerates (resp. decelerates) upwind (resp. downwind) of wave crests. When  $U_{10} = 2.19$ , the contours of  $\tilde{u}/(a_p k_p U_{10})$  and  $\tilde{w}/(a_p k_p U_{10})$  shift at the height of the critical layer  $\zeta_c$  (represented in gray dashed line in panels a, d, and g), where the mean wind speed matches the phase speed of the dominant surface wave [51]: Contours of  $\tilde{u}/(a_p k_p U_{10})$  are “kinked” at  $k_p \zeta = k_p \zeta_c$ , and when  $k_p \zeta < k_p \zeta_c$ ,  $\tilde{w}/(a_p k_p U_{10})$  is negative along upwind wave faces, and positive along downwind wave faces, which is consistent with orbital wave motion (see Sullivan et al. [23], Hristov et al. [52], Grare et al. [39] and Buckley and Veron [26] for details). Estimates of the critical layer heights for all three experiments are listed in Table 1. In these young, strongly wind-forced laboratory waves,

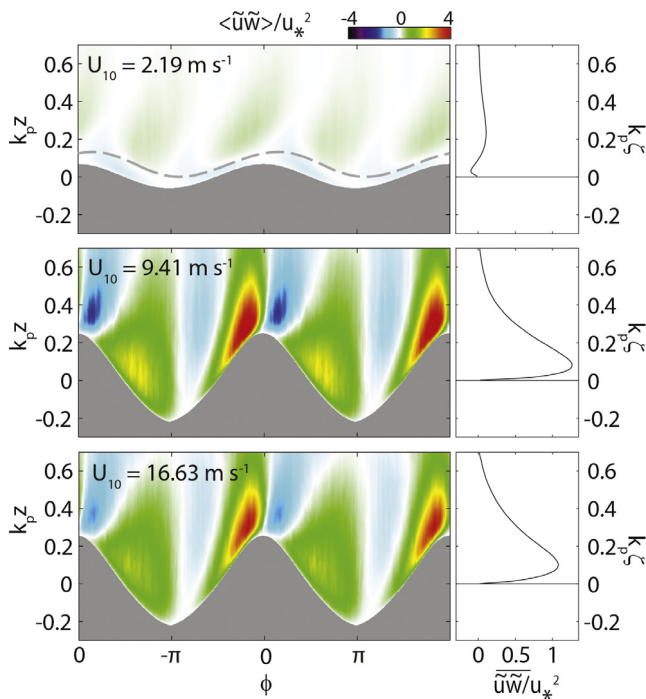


**Fig. 5.** Normalized phase-averaged wave-induced stress  $\langle \tilde{u}\tilde{w} \rangle / u_*^2$  (left) and total mean (across all phases) wave-induced stress  $\overline{\tilde{u}\tilde{w}} / u_*^2$  (right). Phase-averages are plotted above the phase-averaged water surface elevation, and total mean profiles are plotted with respect to the surface following vertical coordinate  $\zeta$ . Each row corresponds to one wind speed with the corresponding mean 10-m wind speeds indicated on the upper left.

the critical height is expected to be very close to the surface. Our measurements show that for  $U_{10} = 2.12, 9.41, 16.63$  m s<sup>-1</sup>, the mean height of the critical layer is respectively 1.84, 0.33, 0.38 mm from the surface. Therefore the critical layer is within or near the viscous sublayer.

### 3.2. Wave induced stress and Reynolds stress

The wave-coherent motions described above generate wave-induced stresses  $\tilde{u}\tilde{w} / u_*^2$ . The phase-averaged and mean profiles of wave-induced stresses are shown in Fig. 5, for the three wind speeds considered. In the two highest wind speed cases ( $U_{10} = 9.41$  and  $16.63$  m s<sup>-1</sup>), the phase-averaged wave-induced stresses are intense and positive above the upwind and downwind faces of the waves, and thin regions of negative stress are found just downwind of crests and troughs. The averaged (across all phases) vertical profiles of wave-induced stress are positive near the surface, and decay to 0 around  $k_p \zeta = 0.7$ . These results are in qualitative agreement with the DNS results of Sullivan et al. [23] for their 0 wave age case (see their Fig. 17 with (“(c/u<sub>\*</sub>, ak) = (0, 0.1)”). This points to the fact that the wind stress above these slow (with respect to the wind speed) very young strongly forced wind waves ( $C_p/u_* = 2.5$  and  $1.4$ ) is similar to that over solid hills. In our slower wind speed case ( $U_{10} = 2.19$  m s<sup>-1</sup>,  $C_p/u_* = 6.5$ ), regions of negative wave stress are found below the critical layer, which, on average across all phases, result in a negative wave stress below the critical layer (see Fig. 7 and accompanying comments below, for a comparison of the wave-induced and turbulent stresses for this wind wave case with the literature).

As described above in Section 2.4, the instantaneous turbulent velocity fields  $\mathbf{u}'$  are obtained by subtracting wave and mean contributions from the measured instantaneous velocity fields.

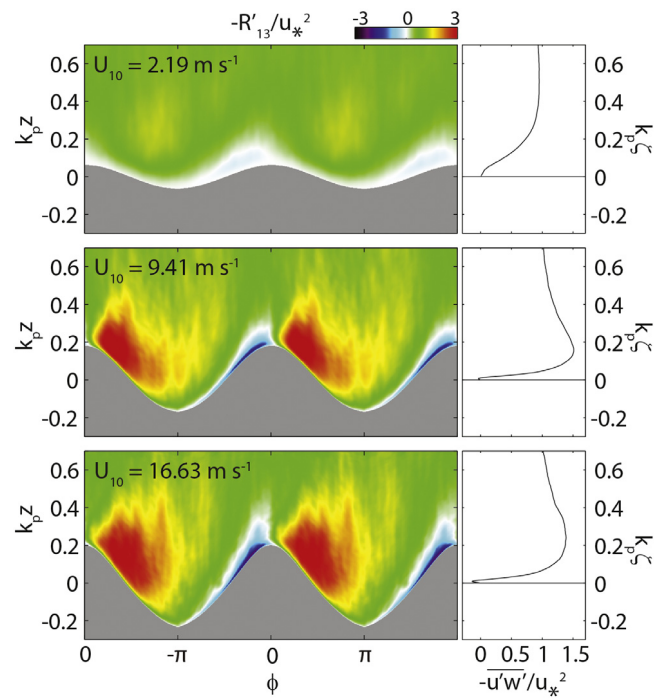


**Fig. 6.** Normalized phase-averaged turbulent stress  $-R'_{13} / u_*^2$  (left) and total mean (across all phases) turbulent stress  $-\overline{u'w'} / u_*^2$  (right). Phase-averages are plotted above the phase-averaged water surface elevation, and total mean profiles are plotted with respect to the surface following vertical coordinate  $\zeta$ . Each row corresponds to one wind speed with the corresponding mean 10-m wind speeds indicated on the upper left.

From these instantaneous turbulent velocities, the Reynolds stress tensor can be readily estimated:

$$\mathbf{R}'(x, \zeta) = \langle \mathbf{u}'(x, \zeta) \otimes \mathbf{u}'(x, \zeta) \rangle, \quad (6)$$

four components of which are directly measured with the PIV. In a first step, we focus on the off-diagonal element  $-R'_{13} = -\langle u'w' \rangle$ , which will be called “turbulent stress” in the remainder of the paper, in accord with classical Reynolds decomposition nomenclature. Fig. 6 shows the normalized, turbulent stress  $-\langle u'w' \rangle / u_*^2$  for  $U_{10}$  wind speeds of 2.19, 9.41, and 16.63 m s<sup>-1</sup>. On the right of the phase-averaged panels, we also show the corresponding ensemble average across all phases  $-\overline{u'w'} / u_*^2$ . At all wind speeds,  $-\langle u'w' \rangle / u_*^2$  displays a strong coupling with the waves. Jet-like regions of strong turbulent stress phase-locked downwind of the waves, which is where the boundary layer is thicker on average. This is in qualitative agreement with the results of Hudson et al. [53], Calhoun and Street [54], Yang and Shen [55]. This average sheltering effect is the result of intermittent separated and non-separated sheltering events. When the turbulent airflow boundary layer separates past wave crests, the resulting free shear layers may dramatically produce turbulence downwind of the airflow-separating crests. Non-separated sheltering events can also cause increased turbulent stress because they are also associated with the generation of free shear layers. These mark the interfaces between swept/ejected regions of high/low horizontal velocity, which are known to occur often in adverse pressure gradient conditions [e.g., 44,56]. It should be noted that the lowest wind speed case ( $U_{10} = 2.19$  m s<sup>-1</sup>) slightly differs from the two others, in that the regions of high turbulent stresses (downwind of crests) are only marginally more intense than the surrounding stresses at other phases. It is likely that these smaller amplitude waves do

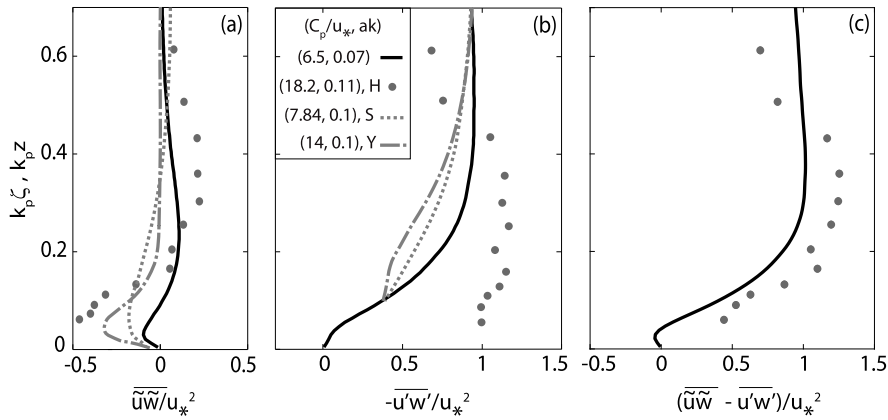


**Fig. 7.** Comparison of our lowest wind speed case's ( $U_{10} = 2.19 \text{ m s}^{-1}$ ) mean wave-induced stress profiles  $\tilde{u}\tilde{w}/u_*^2$  (panel a), mean turbulent stress profiles  $-\overline{u'w'}/u_*^2$  (panel b), and the sum  $(\tilde{u}\tilde{w} - \overline{u'w'})/u_*^2$  (panel c) with the experimental results of Hsu et al. [28] (labeled “H” in the legend), and the DNS results of Sullivan et al. [23] (“S”) and of Yang and Shen [55] (“Y”). All vertical profiles are plotted with respect to the surface following coordinate  $k_p z$ , except the turbulent stress profiles from Sullivan et al. [23] (“S”) and of Yang and Shen [55] (“Y”) in panel b, which were reported with respect to the fixed coordinate  $k_p z$ .

not cause as much turbulence-generating sheltering as the others. Also, over these smaller and slower waves ( $C_p/u_* = 6.5$  for  $U_{10} = 2.19 \text{ m s}^{-1}$ ), we notice a near-surface layer of reduced turbulent stress at all phases. This suggests that within the critical layer, the work of turbulent forces on the waves is reduced. Finally, the systematic reduction in turbulent stress upwind of the crest, suggests that the airflow tends to stabilize and become less turbulent upon approaching wave crests. Flow relaminarization has been observed in aerodynamics, when a flow enters a region of strongly favorable pressure gradient and accelerates [e.g., 56]. Incidentally, aerodynamicists have also observed that in such favorable (negative) pressure gradient conditions, the occurrence of turbulent sweeps and ejections, that are characteristic of turbulent boundary layers, is usually strongly decreased [e.g., 44,56]. For all three wind speeds shown, we observe a thin region of negative turbulent stress near the surface along the upwind face of the waves. This was also observed by Yang and Shen [55] in their direct numerical simulation (DNS) of the airflow over monochromatic waves with  $C_p/u_* \geq 14$ . They suggested that the negative Reynolds stress on the upwind face of the waves is balancing the along-surface horizontal gradient of wave-orbital induced vertical motions in the air. Indeed, Buckley and Veron [26] showed that waves with  $C_p/u_* = 27.7$  induce, on average, important wave-orbital driven vertical motions in the air with downward motions upwind of crests, and upward motions downwind of crests. In this study however, when  $C_p/u_* = 2.5$  and 1.4, the wave-orbital-induced velocities in the air are negligible compared with the “sheltering effect” [21] (see again Fig. 4, e and h for example).

Finally, in Fig. 7, we compare our mean wave-induced stress profiles  $\tilde{u}\tilde{w}/u_*^2$  (panel a), mean turbulent stress profiles  $-\overline{u'w'}/u_*^2$  (panel b), and the sum  $(\tilde{u}\tilde{w} - \overline{u'w'})/u_*^2$  (panel c) with the experimental results of Hsu et al. [28] (labeled “H” in the legend), and the DNS results of Sullivan et al. [23] (“S”) and of Yang and Shen [55] (“Y”). For this comparison, we chose our maximum wave age case  $((C_p/u_*, ak) = (6.5, 0.07))$ , in order to get as close as possible to the experimental conditions from Hsu et al. [28], who used  $(c/u_*, ak) = (18.2, 0.11)$ , for their mechanically generated monochromatic waves. In spite of the young nature of our waves, versus the “intermediate” nature of Hsu et al.’s [28] (see wave age classification in Belcher and Hunt [21] for example), we note a relatively good agreement with our measurements, especially for the sum of wave-induced and turbulent stresses (panel c). Their partitioning of the sum between wave-induced and turbulent stress contributions differs most from ours near the surface, where their turbulent (wave) stress is larger (smaller) than ours (see

panels b and a). It can be noted that the sum becomes relatively constant ( $\approx 1$ ) for  $k_p z > 0.25$ , height below which the viscous contribution may be important. The DNS wave stresses from Sullivan et al. [23] and Yang and Shen [55] (panel a) are qualitatively similar to our measurements, with a negative portion below the critical height, and a positive one above. Panel b shows a general agreement of their turbulent stress profiles (albeit computed with respect to the fixed coordinate  $k_p z$ ) with ours.

### 3.3. Quadrant analysis

In this section, a quadrant analysis [57,58] of turbulent momentum flux events within the buffer layer above wind waves, is presented. Fig. 8 shows the distributions among the four quadrants (defined below) of instantaneous flux events at four different wave phases, for wind waves with  $U_{10} = 2.19, 9.41, 16.63 \text{ m s}^{-1}$ .

We follow a similar methodology to that of Yang and Shen [55] for their DNS study of the airflow over Airy waves: first we present distributions among the four quadrants (defined below) of instantaneous flux events within the airflow’s buffer layer, at four different wave phases (Fig. 8), then we discuss the mean contributions of each quadrant to the mean along-wave turbulent stress (Fig. 9).

An illustration of the quadrant definitions is provided in panel a of Fig. 8. First, it should be noted that the elongated clouds of  $(u', w')$  pairs, point to the anisotropy of the turbulence in the airflow above these strongly forced wind waves, which is generally found in wall-bounded turbulent flows [46]. We do note however that the clouds generally thicken with increasing wind speed (i.e. decreasing wave age and increasing wave slope). The same trend appears in the Airy wave DNS results from Yang and Shen [55] (their Figs. 15 and 14). We generally observe a dominance of Q1–Q3 events upwind of crests (Fig. 8 panels a, e, i), an equivalence of all quadrants above crests (panels b, f, j), a clear dominance of Q2–Q4 events downwind of crests (panels c, g, k), and a very slight dominance of Q2–Q4 events over troughs (panels d, h, l). An exception is noted along the upwind face of waves in the lowest wind speed case (panel a), where the dominance of Q1 and Q3 events is only very slight (slope of linear regression  $\alpha = 0.02$ , not plotted here), probably due to the very small slope of the waves ( $a_p k_p = 0.07$  for  $U_{10} = 2.19 \text{ m s}^{-1}$ ). The Q1–Q3 dominance on the windward side of the waves (where favorable pressure gradient conditions dominate), and the Q2–Q4 dominance on the leeward side of the waves (adverse pressure gradient), is in agreement with past turbulent boundary investigations over solid walls [44,59,56].

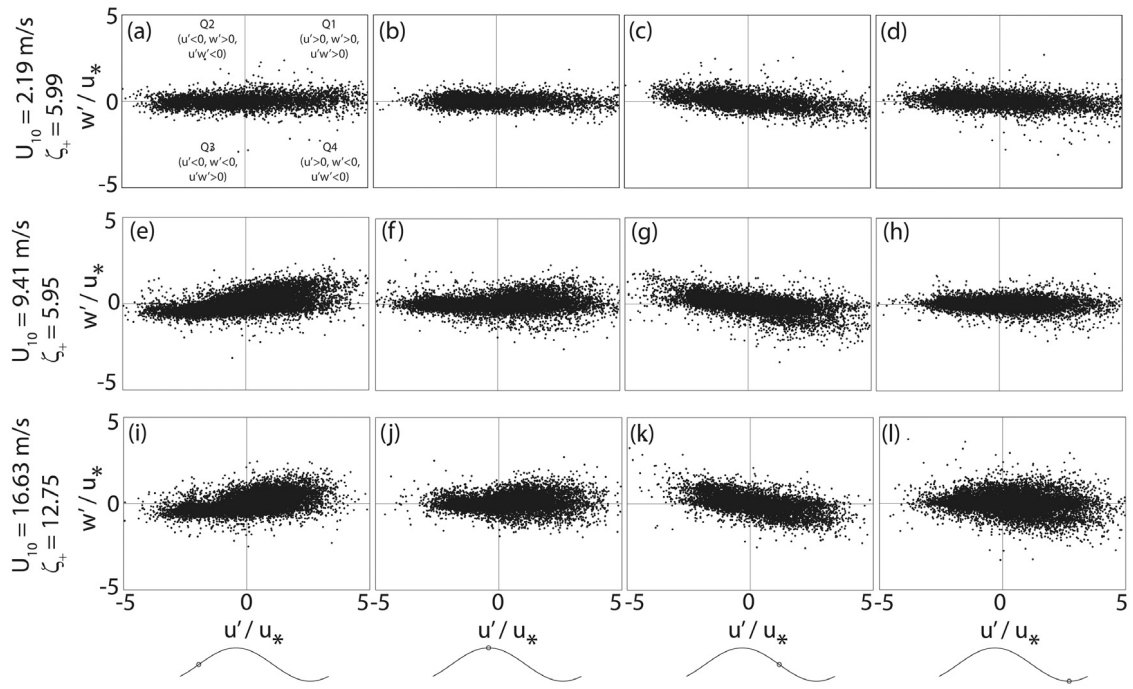


**Fig. 8.** Quadrant distributions of normalized turbulent velocity perturbations,  $w'/u_*$  versus  $u'/u_*$ , above wind waves with  $U_{10} = 2.19 \text{ m s}^{-1}$  (panels a through d),  $9.41 \text{ m s}^{-1}$  (panels e through h), and  $16.63 \text{ m s}^{-1}$  (panels i through l). Turbulent velocities are measured within the airflow's buffer layer above the wavy water surface. As sketched below the plots, four along-wave phase locations are chosen:  $\phi = (-\pi/2, 0, \pi/2, \pi)$ . Quadrants Q1, Q2, Q3, and Q4 are defined in panel a.

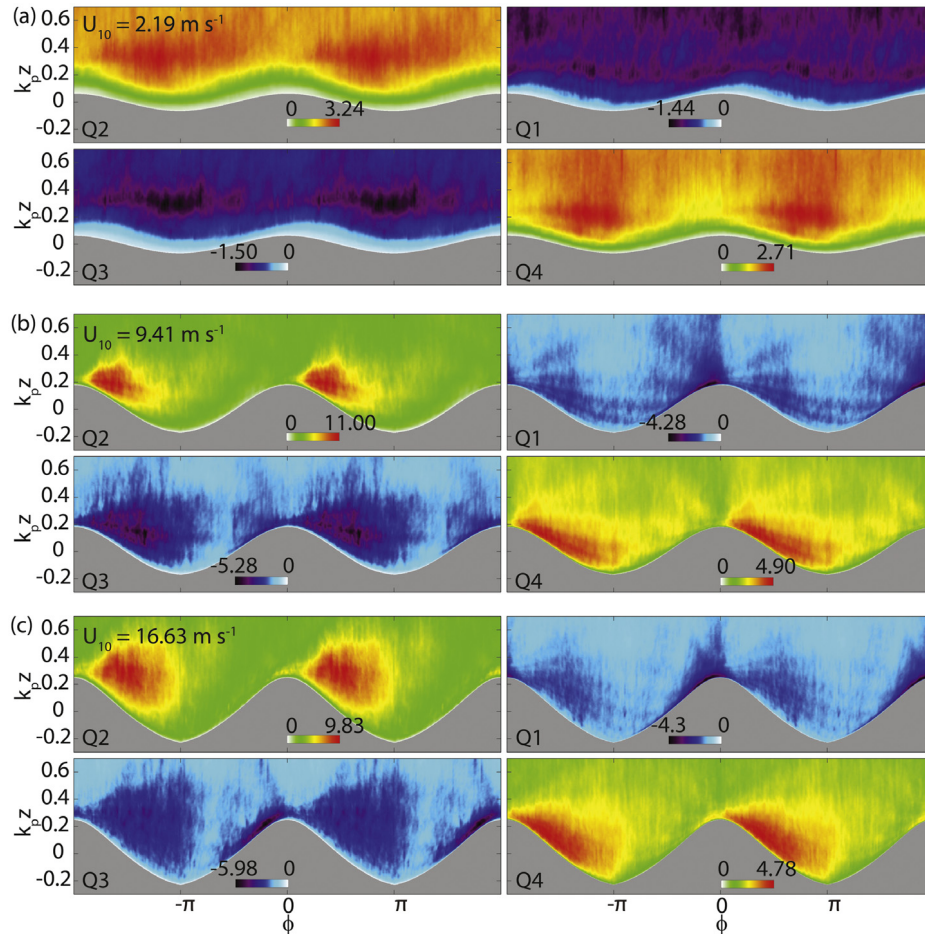


**Fig. 9.** Quadrant contributions to the normalized turbulent stress  $-\langle u'w' \rangle / u_*^2$ , above wind waves for  $U_{10} = 2.19 \text{ m s}^{-1}$  (panel a),  $U_{10} = 9.41 \text{ m s}^{-1}$  (panel b), and  $U_{10} = 16.63 \text{ m s}^{-1}$  (panel c). Q1 and Q3 events are associated with negative momentum flux ( $-u'w' < 0$ ), while Q2 and Q4 events are positive momentum flux events ( $-u'w' > 0$ ).

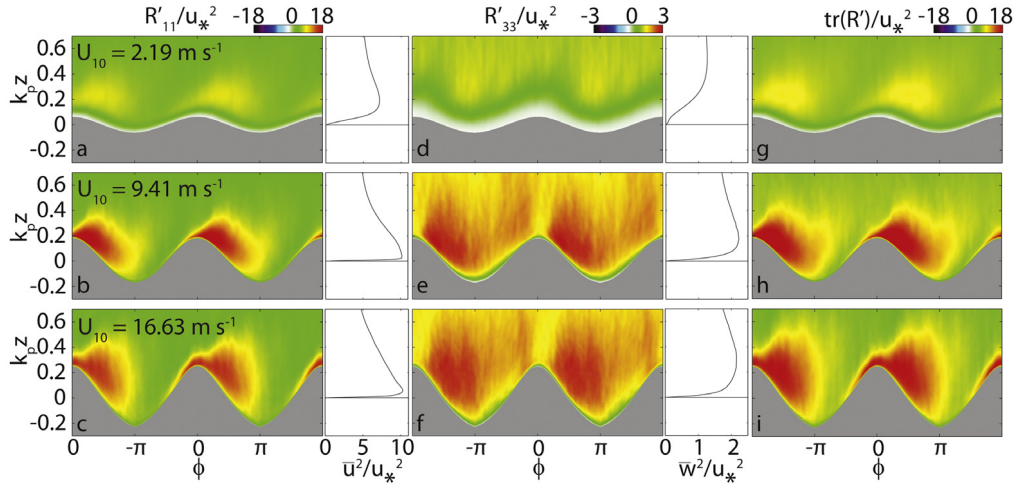


**Fig. 10.** Normalized phase-averaged turbulent velocity variances  $R'_{11}/u_*^2$ ,  $R'_{33}/u_*^2$ . The third column shows  $tr(\mathbf{R}')$  (twice the TKE). Each line of panels is for a different wind speed.

Finally, the patterns observed here are in good qualitative agreement with the DNS simulation results from Yang and Shen [55] (at a height of 5.3 wall units over their young Airy wave case, with  $(c/u_*, ak) = (2, 0.25)$ ). Fig. 9 shows the contributions of each quadrant to the turbulent stresses. In general, both Q2 and Q4 events present the strongest contribution to the turbulent stress  $-\langle u'w' \rangle / u_*^2$ . For  $U_{10} = 9.41$  and  $16.63$  m s<sup>-1</sup>, Q1 and Q3 events have important contributions near the surface just upwind of the crests, which explains the regions of negative turbulent stress in that region (Fig. 6).

### 3.4. Turbulent kinetic energy

In this section, the diagonal elements of the Reynolds stress tensor  $\mathbf{R}'$  are considered. Again, we note that the 2D PIV does not resolve velocities in the spanwise direction. Fig. 10 shows  $R'_{11} = \langle u'^2 \rangle$  and  $R'_{33} = \langle w'^2 \rangle$ . Also, to the right of the phase-averaged fields, we show the ensemble mean profiles of  $\overline{u'^2}$  and  $\overline{w'^2}$ . From the data plotted in Fig. 8, we anticipate  $\langle u'^2 \rangle$  to be generally substantially enhanced compared to  $\langle w'^2 \rangle$ . In fact,  $\frac{\langle u'^2 \rangle}{\langle w'^2 \rangle} \sim O(\bar{\alpha}) \sim O(0.05)$ . This effect is all the more evident close to the interface where vertical velocity fluctuations are expected to be hindered by the presence of the boundary [46]. This simply indicates that the bulk of the turbulent kinetic energy (TKE) is carried by the horizontal velocity variance. A simple estimate of the mean TKE (per unit mass)  $\langle e' \rangle$ , is computed here using the trace of  $\mathbf{R}'$ . Indeed,  $2\langle e' \rangle = \langle |\mathbf{u}'|^2 \rangle = tr(\mathbf{R}')$ . Fig. 10 (last column) shows the resolved  $\langle e' \rangle$  for  $U_{10} = 2.19, 9.41$ , and  $16.63$  m s<sup>-1</sup>. There is on average a phase-locked jet of intense turbulence past the crest of the waves, away from the surface. We attribute this to airflow separation events, whereby high shear layers intermittently detach from the crest of steep waves. Detached (from the surface) free shear layers are sources of intense turbulence away from the surface. It is worth mentioning that although airflow separation only occurs over a fraction (approximately 50%) of all the waves considered to compute the phase-averaged field in Fig. 10h, the turbulence generated by these intermittent events is so intense that it dominates the average. Flow separation past hills has been found to generate an average intensification of the turbulent kinetic energy away from the surface downstream of the hill [e.g., 60,61]. At the lowest wind speed,  $\langle e' \rangle$  is also intensified downwind of crests and away from the surface. Also, above the critical layer, the background turbulence remains relatively high.

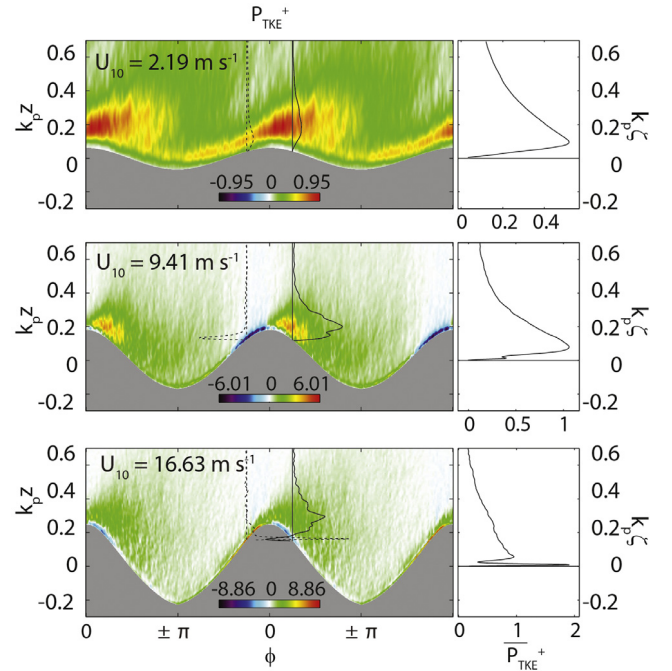


**Fig. 11.** Normalized turbulent kinetic energy production  $P_{TKE}^+ = P_{TKE}/(u_*^2 U_{10} k_p)$ . Profiles with the same scaling factor for all three wind speeds are plotted at phases  $-\pi/4$  and  $\pi/4$ . Ensemble production averages (across all wave phases) are provided on the right of each phase-averaged field.

### 3.5. TKE production

Finally, we examine the production of TKE. The budget equation for the phase-averaged TKE can be written as [62]:

$$\frac{D}{Dt} \langle e' \rangle = \nabla \cdot \left( -\frac{1}{\rho} \langle p' \mathbf{u}' \rangle + 2\nu \langle \mathbf{S}' \cdot \mathbf{u}' \rangle - \langle e' \mathbf{u}' \rangle \right) - \mathbf{R}' : \nabla \langle \mathbf{u} \rangle - 2\nu \langle \mathbf{S}' : \mathbf{S}' \rangle \quad (7)$$

where  $\frac{D}{Dt} = \frac{\partial}{\partial t} + \langle \mathbf{u} \rangle \cdot \nabla$  is the total rate of change, including advection by the mean (phase-averaged) flow  $\langle \mathbf{u} \rangle$ . The turbulent strain rate tensor is  $\mathbf{S}' = \frac{1}{2} (\nabla \mathbf{u}' + (\nabla \mathbf{u}')^T)$ , where  $\nabla \mathbf{u}'$  is the

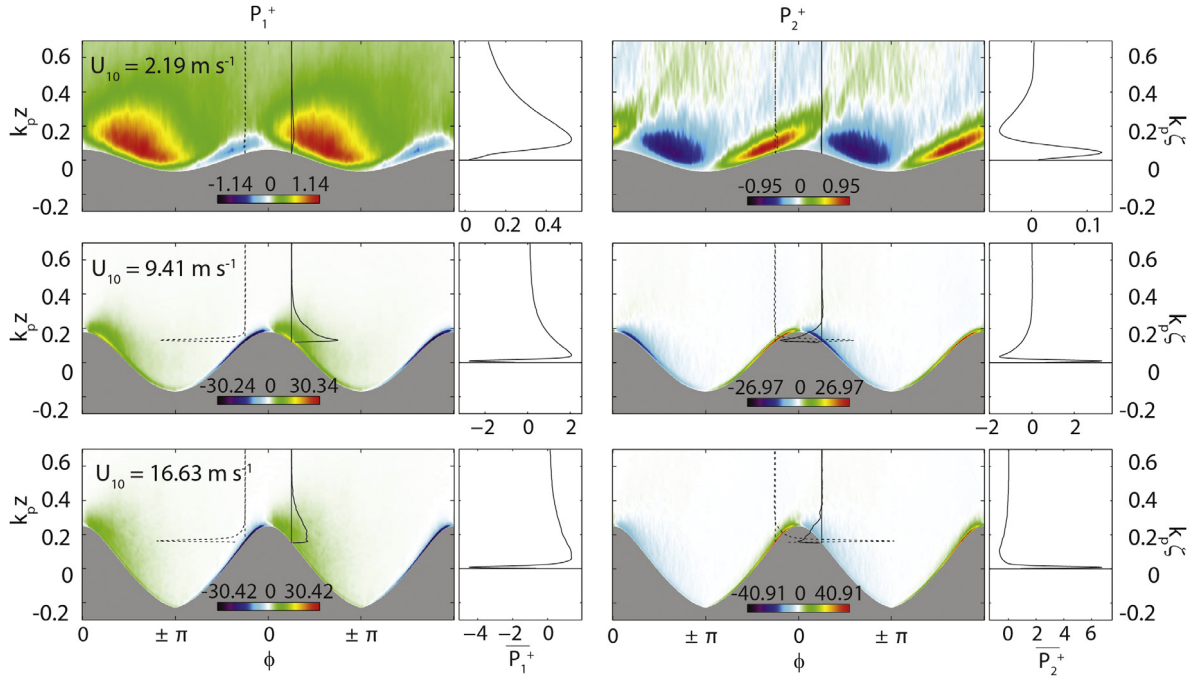


**Fig. 12.** Two largest normalized turbulent kinetic energy (TKE) production terms  $P_1^+ = P_1/[u_*^2(U_{10}k_p)]$  and  $P_2^+ = P_2/[u_*^2(U_{10}k_p)]$ . See additional comments in the caption of Fig. 11.

gradient velocity tensor and  $(\nabla \mathbf{u}')^T$  its transpose. In Eq. (7), the divergence term on the right hand side represents transport of TKE. The three terms within, in order, are the pressure transport, viscous transport, and turbulent transport terms. Below, the second term involving the inner product of the Reynolds stress tensor  $\mathbf{R}'$  with the gradient of the mean flow  $\nabla(\mathbf{u})$ , is the turbulent production term. The last term on the right hand side of Eq. (7) is the viscous dissipation of TKE. The TKE production  $P_{TKE} = -\mathbf{R}' : \nabla(\mathbf{u})$  is presented in Fig. 11, for  $U_{10} = 2.19, 9.41,$  and  $16.63 \text{ m s}^{-1}$ . Phase-averages are on the left, and means across all phases are on the right. Color plots are provided to show the along-wave distribution of TKE production. Note here that we have normalized the TKE production  $P_{TKE}^+ = P_{TKE}/u_*^2 U_{10} k_p$  but that despite the normalization, we have plotted different wind conditions with using a color scheme adapted to each data range. Profiles with the same scaling factor for all five experiments are plotted at phases  $-\pi/4$  and  $\pi/4$ , in order to better show the differences in magnitude from one experiment to another. At the lowest wind speed ( $U_{10} = 2.19 \text{ m s}^{-1}$ ), nearly no TKE is produced near the surface, within the critical layer. Upwind of the wave crest, intense TKE is produced within a thin region located at the top of the critical layer. Just before the wave crest, the high TKE production region begins to expand into a jet-like contour, which then extends past the crest onto the downwind face of the average wave, up to  $\phi \approx \pi/2$ . We attribute this expansion of the high TKE region to the bursts of high spanwise vorticity (and high shear) layers away from the surface, that occur frequently in adverse pressure gradient conditions, over the downwind face of the waves. These free shear layers are known to be sources of intense TKE production [63]. When  $U_{10} = 9.41 \text{ m s}^{-1}$ , once again,  $P_{TKE}$  is large downwind of the crest where airflow separation presumably plays an important role. However in this case, the TKE is dramatically destroyed ( $P_{TKE} < 0$ ) very near the surface, just upwind of the crest. This can be explained by the intense boundary layer thinning that occurs in that region of highly favorable pressure gradient. In that region, near the smooth water surface upwind of the crest, turbulent motions are reduced, and viscous dissipation is important. In fact, the water surface is generally smooth upwind of crests and the viscous sublayer intact.

The entire sampled air column above  $\phi \sim -\pi/4$  experiences either TKE destruction or at least very weak production. This result is coherent with the hypothesis of a tendency toward relaminarization of the airflow upon approaching the crest (see above). At the highest wind speeds ( $U_{10} = 16.63 \text{ m s}^{-1}$ ), there is no inner layer free of TKE production. It should be noted that no critical layer was observed at this wind speed because the waves are too young (see Buckley and Veron [26]). We also note a very thin layer of negative  $P_{TKE}$  at the surface past wave crests. This suggests that airflow separation is causing this near surface region to be so sheltered that TKE is destroyed, probably by viscous forces very close to the sheltered surface. Notice that even at lower wind speeds, no TKE is ever produced in that very thin, near-surface, sheltered region. At this wind speed, and unlike in the two lower wind speed cases, there is also a peak in TKE production on the upwind face of the waves, on average. In that region,  $P_{TKE}$  even exceeds the TKE production caused by airflow separation. We believe this to be caused by the surface roughness that is, visually at least (on individual LIF images, not shown here), significantly different and enhanced compared to more moderate winds of  $U_{10} < O(10) \text{ m s}^{-1}$ . The production of TKE can be further decomposed in several resolved components.

$$P_{TKE} = \underbrace{-\langle u'w' \rangle \frac{\partial \langle u \rangle}{\partial z}}_{P_1} - \underbrace{\langle u^2 \rangle \frac{\partial \langle u \rangle}{\partial x}}_{P_2} - \underbrace{\langle w^2 \rangle \frac{\partial \langle w \rangle}{\partial z}}_{P_3} - \underbrace{\langle u'w' \rangle \frac{\partial \langle w \rangle}{\partial x}}_{P_4}. \quad (8)$$

Fig. 12 shows  $P_1$  and  $P_2$  (normalized) which are the two largest contributing terms to the total TKE production. Also, Fig. 13 shows  $P_3$  and  $P_4$  (normalized) which are one to two orders of magnitude smaller than  $P_1$  and  $P_2$ . This means that  $P_1$  and  $P_2$  are the principal contributors to the total TKE production  $P_{TKE}$  (Fig. 11). A general observation is that  $P_1$  and  $P_2$  compete against each other, and  $P_3$  and  $P_4$  do so as well. Interestingly, these terms show similar features at all wind speeds:  $P_1$  is negative on the upwind face of waves, and positive on downwind faces, whereas  $P_2$  shows the opposite pattern (Fig. 12). Yet the total TKE production  $P_{TKE}$  is relatively different from one experiment to another (see comments

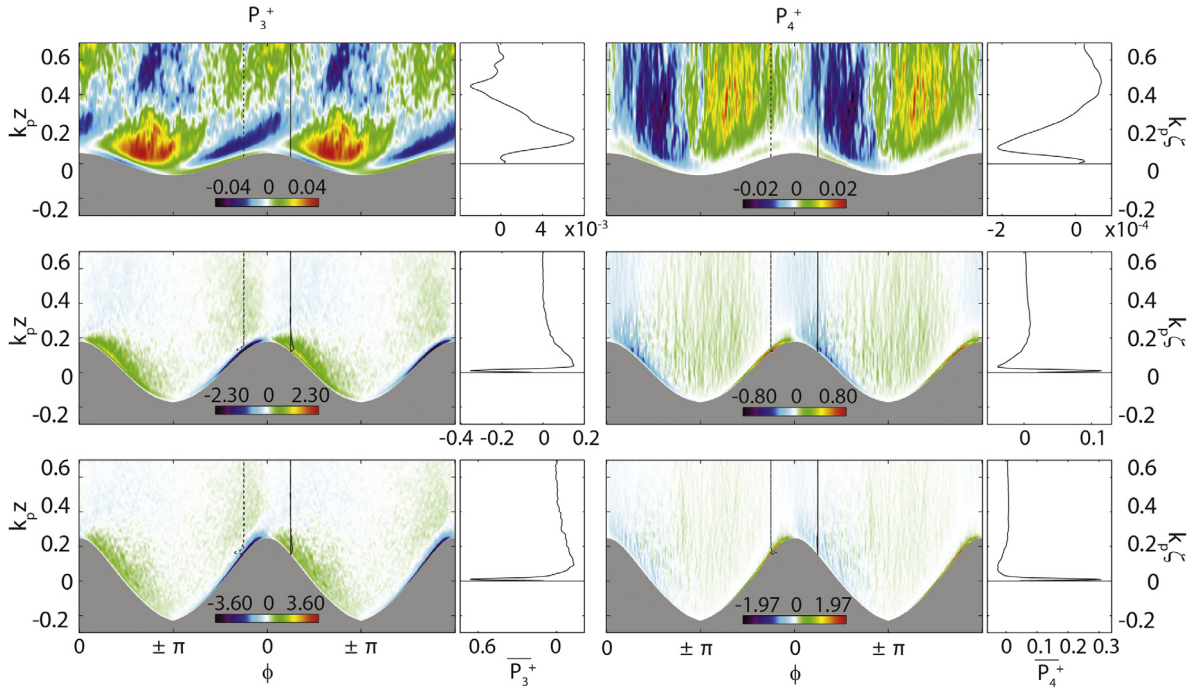


**Fig. 13.** Two smallest normalized turbulent kinetic energy (TKE) production terms  $P_3^+ = P_3/[u_*^2 (U_{10}k_p)]$  and  $P_4^+ = P_4/[u_*^2 (U_{10}k_p)]$ . See additional comments in the caption of Fig. 12.

above). This means that it is the competition between the along-wave magnitudes of  $P_1$  and  $P_2$  that determines the total production  $P_{TKE}$ . Broadly, we notice that with increasing wind speed, the magnitudes of  $P_2$  start off smaller than those of  $P_1$  (from  $U_{10} = 2.19$  to  $9.41 \text{ m s}^{-1}$ ), and gradually take over and become larger than the magnitudes of  $P_1$  at high wind speeds ( $U_{10} = 16.63 \text{ m s}^{-1}$ ). This effect is also noticeable when looking again at the total TKE production  $P_{TKE}$  in Fig. 11: at the intermediate wind speed case ( $U_{10} = 9.41 \text{ m s}^{-1}$ ),  $P_{TKE}$  is negative on upwind wave faces, and positive downwind (just like  $P_1$ , in Fig. 12, left). At the highest wind speeds, the trend is opposite:  $P_{TKE}$  is positive upwind of crests, and negative at the surface downwind of crests (like  $P_2$ , Fig. 12, right). Away from the surface however, above downwind oriented wave faces,  $P_{TKE}$  is always positive, i.e., it is controlled by the  $P_1$  term. This is probably connected to the phase locked sheltering (separated or not) that occurs systematically past wave crests. The  $P_3$  and  $P_4$  terms are also competing against one another:  $P_3$  (Fig. 13, left) is generally negative along upwind wave faces, and positive downwind. The opposite is true for the smallest term  $P_4$  (Fig. 13, right). However in this case, the smallest term (right) remains approximately 50% smaller than the  $\langle w'^2 \rangle$  producing term, and this for all wind speeds. Overall, it is clear that  $P_1$  and  $P_2$  (and also  $P_3$  and  $P_4$ ) compete against each other because of the features in the mean gradients  $\frac{\partial \langle u \rangle}{\partial z}$  and  $\frac{\partial \langle u \rangle}{\partial x}$ . Indeed,  $\langle u \rangle = \bar{u} + \tilde{u}$ , thus in the absence of mean flow and with linear wave induced (orbital) motion, these gradient fields would be exactly orthogonal. Under these circumstances, and in a spatially homogeneous turbulent field,  $P_1$  and  $P_2$  would entirely compensate. Here,  $\langle u'w' \rangle$  and  $\langle u'^2 \rangle$  are not homogeneous and of course,  $\frac{\partial \langle u \rangle}{\partial z} = \frac{\partial \bar{u}}{\partial z} + \frac{\partial \tilde{u}}{\partial z}$ . Furthermore, since  $\bar{w} = 0$ , the  $P_3$  and  $P_4$  terms only involve the gradients of the mean wave-coherent vertical velocity  $\frac{\partial \bar{w}}{\partial z}$ . While we anticipate that  $\frac{\partial \bar{u}}{\partial z}$  to be larger in magnitude than  $\frac{\partial \bar{w}}{\partial z}$ , the reason for the differences in the scaling of  $P_1$ ,  $P_2$ ,  $P_3$  and  $P_4$  remains obscured at this stage of the analysis. However, we suggest that the triple decomposition outlined in Eq. (4) will prove useful in estimating terms in the TKE balance equation that are related to the advection or production of TKE by the wave-coherent velocity and velocity gradients. A

more complete examination of these wave-induced effects is the subject of ongoing analysis and will be presented in a subsequent publication.

#### 4. Conclusions

In this paper, we have presented high resolution quantitative velocity measurements in the turbulent airflow above surface waves and down to within the viscous sublayer. We were able to achieve high resolution two-dimensional velocity measurements in the airflow above wind waves, in a range of 10-m extrapolated wind speeds from  $2.19 \text{ m s}^{-1}$  to  $16.63 \text{ m s}^{-1}$ . Our measurements resolved velocities as close as  $100 \mu\text{m}$  above the water surface. We identified coherent turbulent structures in the airflow above waves, that have been, up to now, only observed above solid walls [64]: bursts of near surface spanwise vorticity, and turbulent ejections and sweeps. Airflow separation events, also directly observed, start to appear in low to moderate winds, and are very frequent at high wind speeds. They occur over nearly 90% of the short wind waves at  $U_{10} = 16.63 \text{ m s}^{-1}$ . By phase averaging velocities and fluxes within the airflow, we were able to quantify the mean dynamics within the viscous sublayer, buffer and logarithmic layers, as well as below and above the critical height. We found evidence of turbulent boundary layer thinning and thickening over wind waves. Airflow separation dramatically influences instantaneous and mean along-wave stress distributions. This effect is most pronounced when viscous sublayers exist upwind of crests. This is observed only up to certain wind speeds (here up to  $U_{10} = 9.41 \text{ m s}^{-1}$ ). At higher wind speeds, intense turbulent kinetic energy is present along the entire wave profile. We also note that at the lowest wind speed  $U_{10} = 2.19 \text{ m s}^{-1}$ , the mean properties of the airflow are considerably different within a thin region near the surface (below the critical height), from the behavior farther away from the surface (outside the critical layer). This result is in agreement with previous modeling efforts [21,23,24,55]. Finally, the production of turbulent kinetic energy does not appear to scale with common boundary layer quantities (wind speed, friction

velocity) in a trivial way, and across wind and wave conditions. In fact, the resolved components of the turbulent kinetic energy production indicate that a cautious accounting for wave-related effects might be necessary.

## Acknowledgments

We would like to thank Mathieu Colin, Pierre Lubin, Henrik Kalisch, Mario Ricchiuto, and Magnus Svård for organizing the B'Waves conferences in Bordeaux, France, in 2014 and Bergen, Norway, in 2016 and for arranging for this special issue of the European Journal of Mechanics. This work was supported by US National Science Foundation grants OCE-1458977, OCE-1233808, OCE 0748767, and AGS-PRF-1524733.

## References

- [1] D. Turney, S. Banerjee, Transport phenomena at interfaces between turbulent fluids, *AIChE J.* (2008).
- [2] G. Hewitt, *Annular Two-Phase Flow*, Elsevier, 2013.
- [3] M.D. Powell, P.J. Vickery, T.A. Reinhold, Reduced drag coefficient for high wind speeds in tropical cyclones, *Nature* 422 (2003) 279–283.
- [4] M.A. Donelan, B.K. Haus, N. Reul, W.J. Plant, M. Stiassni, H.C. Graber, O.B. Brown, E.S. Saltzman, On the limiting aerodynamic roughness of the ocean in very strong winds, *Geophys. Res. Lett.* 31 (2004).
- [5] M.M. Bell, M.T. Montgomery, K.A. Emanuel, Air-sea enthalpy and momentum exchange at major hurricane wind speeds observed during CBLAST, *J. Atmos. Sci.* 69 (2012) 3197–3222.
- [6] A.V. Soloviev, R. Lukas, M.A. Donelan, B.K. Haus, I. Ginis, The air-sea interface and surface stress under tropical cyclones, *Sci. Rep.* 4 (2014).
- [7] F. Veron, Ocean spray, *Annu. Rev. Fluid Mech.* 47 (2015) 507–538.
- [8] P.P. Sullivan, J.C. McWilliams, Dynamics of winds and currents coupled to surface waves, *Annu. Rev. Fluid Mech.* 42 (2010) 19–42.
- [9] G. Deane, M.D. Stokes, Scale dependence of bubble creation mechanisms in breaking waves, *Nature* 418 (2002) 839–844.
- [10] R.J. Rapp, W.K. Melville, Laboratory measurements of deep-water breaking waves, *Phil. Trans. R. Soc. A* 331 (1990) 735–800.
- [11] W.K. Melville, The role of surface-wave breaking in air-sea interaction, *Annu. Rev. Fluid Mech.* 28 (1996) 279–321.
- [12] W.K. Melville, F. Veron, C.J. White, The velocity field under breaking waves: Coherent structures and turbulence, *J. Fluid Mech.* 454 (2002) 203–233.
- [13] D.A. Drazen, W.K. Melville, Turbulence and mixing in unsteady breaking surface waves, *J. Fluid Mech.* 628 (2009) 85–119.
- [14] M. Perlin, W. Choi, Z. Tian, Breaking waves in deep and intermediate waters, *Annu. Rev. Fluid Mech.* 45 (2013) 115–145.
- [15] A.S. Monin, A.M. Obukhov, Basic laws of turbulent mixing in the surface layer of the atmosphere, *Trudy Geofiz. Inst. Aca. Nauk SSSR* 24 (1954) 163–187.
- [16] H. Schlichting, K. Gersten, *Boundary-Layer theory*, Springer, 2000.
- [17] I. Jones, Y. Toba, *Wind Stress Over the Ocean*, Cambridge University Press, 2001, p. 303.
- [18] C.W. Fairall, E.F. Bradley, J.E. Hare, A.A. Grachev, J.B. Edson, Bulk parameterization of air-sea fluxes: Updates and verification for the COARE algorithm, *J. Clim.* 16 (2003) 571–591.
- [19] J.B. Edson, V. Jampana, R. a. Weller, S.P. Bigorre, A.J. Plueddemann, C.W. Fairall, S.D. Miller, L. Mahrt, D. Vickers, H. Hershbach, On the exchange of momentum over the open ocean, *J. Phys. Oceanogr.* 43 (2013) 1589–1610.
- [20] S.E. Belcher, J.C.R. Hunt, Turbulent shear flow over slowly moving waves, *J. Fluid Mech.* 251 (1993) 119–148.
- [21] S.E. Belcher, J.C.R. Hunt, Turbulent flow over hills and waves, *Annu. Rev. Fluid Mech.* 30 (1998) 507–538.
- [22] A. Smedman, U. Högström, H. Bergström, A. Rutgersson, K.K. Kahma, H. Pettersson, A case study of air-sea interaction during swell conditions, *J. Geophys. Res.* 104 (1999) 25833–25851.
- [23] P.P. Sullivan, J.C. McWilliams, C. Moeng, Simulation of turbulent flow over idealized water waves, *J. Fluid Mech.* 404 (2000) 47–85.
- [24] N. Kihara, H. Hanazaki, T. Mizuya, H. Ueda, Relationship between airflow at the critical height and momentum transfer to the traveling waves, *Phys. Fluids* 19 (2007) 015102.
- [25] P.P. Sullivan, J.B. Edson, T. Hristov, J.C. McWilliams, Large-eddy simulations and observations of atmospheric marine boundary layers above nonequilibrium surface waves, *J. Atmos. Sci.* 65 (2008) 1225–1245.
- [26] M.P. Buckley, F. Veron, Structure of the airflow above surface waves, *J. Phys. Oceanogr.* 46 (2016) 1377–1397.
- [27] P.P. Sullivan, M.L. Banner, R.P. Morison, W.L. Peirson, Turbulent flow over steep steady and unsteady waves under strong wind forcing, *J. Phys. Oceanogr.* 48 (2018) 3–27.
- [28] C. Hsu, E. Hsu, R. Street, On the structure of turbulent flow over a progressive water wave: Theory and experiment in a transformed, wave-following coordinate system, *J. Fluid Mech.* 105 (1981) 87–117.
- [29] M.L. Banner, W.K. Melville, On the separation of air flow over water waves, *J. Fluid Mech.* 77 (1976) 825–842.
- [30] P.R. Gent, P.A. Taylor, A note on separation over short wind waves, *Boundary-layer meteorol.* 11 (1977) 65–87.
- [31] S. Kawai, Structure of air flow separation over wind wave crests, *Bound.-Lay. Meteorol.* 23 (1982) 503–521.
- [32] N. Reul, H. Branger, J.-P. Giovanangeli, Air flow separation over unsteady breaking waves, *Phys. Fluids* 11 (1999) 1959–1961.
- [33] F. Veron, G. Saxena, S.K. Misra, Measurements of the viscous tangential stress in the airflow above wind waves, *Geophys. Res. Lett.* 34 (2007).
- [34] N. Reul, H. Branger, J.-P. Giovanangeli, Air flow structure over short-gravity breaking water waves, *Bound.-Lay. Meteorol.* 126 (2008) 477–505.
- [35] J.L. Lumley, E.A. Terray, Kinematics of turbulence convected by a random wave field, *J. Phys. Oceanogr.* 13 (1983) 2000–2007.
- [36] L. Thais, J. Magnaudet, Turbulent structure beneath surface gravity waves sheared by the wind, *J. Fluid Mech.* 328 (1996) 313–344.
- [37] T. Hristov, C.A. Friehe, S. Miller, Wave coherent fields in the air flow over ocean waves: Identification of cooperative behavior buried in turbulence, *Phys. Rev. Lett.* 81 (1998) 5245–5248.
- [38] F. Veron, W.K. Melville, L. Lenain, Wave-coherent air-sea heat flux, *J. Phys. Oceanogr.* 38 (2008) 788–802.
- [39] L. Grare, L. Lenain, W.K. Melville, Wave-coherent airflow and critical layers over ocean waves, *J. Phys. Oceanogr.* 43 (2013) 2156–2172.
- [40] M.P. Buckley, *Structure of the Airflow Above Surface Waves* (Ph.D. dissertation), University of Delaware, 2015, p. 152.
- [41] M.P. Buckley, F. Veron, Airflow measurements at a wavy air-water interface using PIV and LIF, *Exp. Fluids* 58 (2017) 161.
- [42] M. Thomas, S. Misra, C. Kambhamettu, J.T. Kirby, A robust motion estimation algorithm for PIV, *Meas. Sci. Technol.* 16 (2005) 865–877.
- [43] J. Duncan, H. Qiao, V. Philomin, A. Wenz, Gentle spilling breakers: Crest profile evolution, *J. Fluid Mech.* 379 (1999) 191–222.
- [44] S.J. Kline, W.C. Reynolds, F.A. Schraub, P.W. Runstadler, The structure of turbulent boundary layers, *J. Fluid Mech.* 30 (1967) 741–773.
- [45] S.K. Robinson, Coherent motions in the turbulent boundary layer, *Annu. Rev. Fluid Mech.* 23 (1991) 601–639.
- [46] J. Jiménez, Cascades in wall-bounded turbulence, *Annu. Rev. Fluid Mech.* 44 (2011) 27.
- [47] R.L. Simpson, Turbulent boundary layer separation, *Annu. Rev. Fluid Mech.* 21 (1989) 205–234.
- [48] T. Hara, P.P. Sullivan, Wave boundary layer turbulence over surface waves in a strongly forced condition, *J. Phys. Oceanogr.* 45 (2015) 868–883.
- [49] A.K.M.F. Hussain, W.C. Reynolds, The mechanics of an organized wave in turbulent shear flow, *J. Fluid Mech.* 41 (1970) 241–258.
- [50] O.M. Phillips, *The Dynamics of the Upper Ocean*, Cambridge University Press, 1977, p. 261.
- [51] J. Miles, On the generation of surface waves by shear flows, *J. Fluid Mech.* 3 (1957) 185–204.
- [52] T. Hristov, S. Miller, C. Friehe, Dynamical coupling of wind and ocean waves through wave-induced air flow, *Nature* 422 (2003) 55–58.
- [53] J. Hudson, L. Dykhn, T. Hanratty, Turbulence production in flow over a wavy wall, *Exp. Fluids* 20 (1996) 257–265.
- [54] R.J. Calhoun, R.L. Street, Turbulent flow over a wavy surface: Neutral case, *J. Geophys. Res.* 106 (2001) 9277–9294.
- [55] D. Yang, L. Shen, Direct-simulation-based study of turbulent flow over various waving boundaries, *J. Fluid Mech.* 650 (2010) 131–180.
- [56] L.S. Kovaszny, The turbulent boundary layer, *Annu. Rev. Fluid Mech.* 2 (1970) 95–112.
- [57] J.M. Wallace, H. Eckelmann, R.S. Brodkey, The wall region in turbulent shear flow, *J. Fluid Mech.* 54 (1972) 39–48.
- [58] W. Willmarth, S. Lu, Structure of the Reynolds stress near the wall, *J. Fluid Mech.* 55 (1972) 65–92.
- [59] J. Kim, P. Moin, R. Moser, Turbulence statistics in fully developed channel flow at low Reynolds number, *J. Fluid Mech.* 177 (1987) 133–166.
- [60] J.A. Palmer, R. Mejia-Alvarez, J.L. Best, K.T. Christensen, Particle-image velocimetry measurements of flow over interacting barchan dunes, *Exp. Fluids* 52 (2012) 809–829.
- [61] S.E. Belcher, A.L.M. Grant, K.E. Hanley, B. Fox-Kemper, L. Van Roekel, P.P. Sullivan, W.G. Large, A. Brown, A. Hines, D. Calvert, A. Rutgersson, H. Pettersson, J.-R. Bidlot, P.A.E.M. Janssen, J.A. Polton, A global perspective on langmuir turbulence in the ocean surface boundary layer, *Geophys. Res. Lett.* 39 (2012).
- [62] W.C. Reynolds, A.K.M.F. Hussain, The mechanics of an organized wave in turbulent shear flow. Part 3. Theoretical models and comparisons with experiments, *J. Fluid Mech.* 54 (1972) 263288.
- [63] C.-M. Ho, P. Huerre, Perturbed free shear layers, *Annu. Rev. Fluid Mech.* 16 (1984) 365–422.
- [64] R.J. Adrian, Hairpin vortex organization in wall turbulence, *Phys. Fluids* 19 (2007) 041301.